Accepted Article

Title: Surface Degradation of Single-crystalline Ni-rich Cathode and Regulation Mechanism by Atomic Layer Deposition in Quasi-Solid-State Lithium Batteries

Authors: Huijuan Guo, Yipeng Sun, Yang Zhao, Gui-Xian Liu, Yue-Xian Song, Jing Wan, Ke-Cheng Jiang, Yu-Guo Guo, Xueliang Sun, and Rui Wen

This manuscript has been accepted after peer review and appears as an Accepted Article online prior to editing, proofing, and formal publication of the final Version of Record (VoR). The VoR will be published online in Early View as soon as possible and may be different to this Accepted Article as a result of editing. Readers should obtain the VoR from the journal website shown below when it is published to ensure accuracy of information. The authors are responsible for the content of this Accepted Article.

WILEY-VCH

Surface Degradation of Single-crystalline Ni-rich Cathode and Regulation Mechanism by Atomic Layer Deposition in Quasi-Solid-State Lithium Batteries

Hui-Juan Guo+,[a, b, c] Yipeng Sun+,[d] Yang Zhao,[d] Gui-Xian Liu,[a, c] Yue-Xian Song,[a, c] Jing Wan,[a, c] Ke-Cheng Jiang,[e] Yu-Guo Guo,[a, c] Xueliang Sun*,[d] and Rui Wen*[a, c]

[a][*]   Dr. H.-J. Guo, G.-X. Liu, Y.-X. Song, J. Wan, Prof. Dr. R. Wen, Prof. Dr. Y.-G. Guo
         Key Laboratory of Molecular Nanostructure and Nanotechnology, Beijing National Laboratory for Molecular Sciences, CAS Research/Education Center for
         Excellence in Molecular Sciences, Institute of Chemistry, Chinese Academy of Sciences,
         Beijing 100190, P. R. China
         E-mail: ruiwen@iccas.ac.cn, xsun@eng.uwo.ca
[b]   Dr. H.-J. Guo
         Key Laboratory of Green Chemical Engineering Process of Ministry of Education, School of Chemical Engineering and Pharmacy, Wuhan Institute of
         Technology,
         Wuhan 430072, P. R. China
[c]   Dr. H.-J. Guo, G.-X. Liu, Y.-X. Song, J. Wan, Prof. Dr. Y.-G. Guo, Prof. Dr. R. Wen
         University of the Chinese Academy of Sciences (China),
         Beijing 100049, P. R. China
[d]   Y. P. Sun, Dr. Y. Zhao, Prof. Dr. X. L. Sun
         Department of Mechanical and Materials Engineering, University of Western Ontario,
         London, Ontario, N6A 5B9, Canada
[e]   K.-C Jiang
         Dongguan TAFEL New Energy Technology Company, Limited,
         Dongguan 523000, P.R. China;
[+]   These authors contributed equally to this work.

         Supporting information for this article is given via a link at the end of the document.

Abstract: Single-crystalline Ni-rich cathode (SC-NCM) has attracted increasing interest owing to its greater capacity retention in advanced solid-state lithium batteries (SSLBs), while suffers from severe structural instability during cycling. Here, via atomic layer deposition, Li_3PO_4 is introduced to coat SC-NCM (L-NCM), to suppress side reaction and enhance interfacial stability. The dynamic degradation and surface regulation of SC-NCM are investigated inside a working SSLB by *in situ* atomic force microscopy (AFM). We directly observe the uneven cathode electrolyte interphase (CEI) and surface defects on surface of pristine SC-NCM particle. Remarkably, the formed amorphous LiF-rich CEI on L-NCM maintains the initial structure of SC-NCM, and thus endows the battery with improved cycling stability and excellent rate capability. Such on-site tracking provides deep insights into surface mechanism and structure−reactivity correlation of SC-NCM, and thus benefits the optimizations of SSLBs.

Introduction

Future generations of electrical vehicles have promoted the rapidly increasing demands for high-energy-density battery systems.[1] Solid-state lithium batteries (SSLBs) demonstrate great potential for electric vehicles and portable electronics, due to higher energy density and superior safety performance.[2] In SSLBs, the collocation of the Ni-rich layer oxide ($LiNi_xCo_yMn_{1−x−y}O_2$, NCM, $x \geq 0.5$) cathode and the Li anode is the most promising approach to achieve an energy density higher than 300 Wh kg^{-1}. However, the inferior chemical compatibility and poor interface stability between cathode and solid electrolyte are prone to cause battery performances degradation, hindering its further extensive application.[3] Moreover, traditional layered oxide cathode always suffers from a significant degradation process due to intragranular cracking, particle crack formation, and structural transformations.[4] To solve these problems, creative strategies are necessary to restrict structural failure and improve structural stability of cathode particles.

Studies have been focused on the single-crystalline Ni-rich layer oxide cathode of SSLBs due to their superior capacity retention during long cycle times compared with the conventional polycrystalline battery particles.[5] Single-crystalline NCM cathode with only one grain for one particle can address the challenges present in its polycrystalline counterpart by reducing phase boundaries and materials surfaces.[6] On the one hand, in theory, single-crystalline NCM cathode tends to provide increased oxygen loss resistance and sound structural stability in interactions with electrolyte without grain boundaries in particles.[7] On the other hand, intergranular cracks are induced by the nonuniform volume change of primary particles during cycling, and exacerbated by the anisotropic lattice expansion/contraction among individual particles and grains in the polycrystalline cathode.[8] The single-crystalline cathode can suppress these cracking problem duo to its exhibited intrinsic integrity. Although single-crystalline NCM cathode that shows good performance has been demonstrated, degradations from single-crystalline Ni-rich cathodes still occur and intrinsically hinder the further improvement of practical applications.[9] Intensive investigation of the degradation mechanism of single-crystalline Ni-rich cathode, exploring effective modification technologies, are critical in designing advanced electrode materials with better performance and stability.[10]

For the sake of performance enhancements of the single-crystalline Ni-rich cathode based SSLBs, the surface modification of cathode has been proved as an effective method to alleviate the side-reactions, enhance Li$^+$ transfer efficiency and

stabilize the cathode/electrolyte interface.[11] In response, various materials, such as metal oxides, phosphates and fluorides have been explored.[3c, 12] Atomic layer deposition (ALD) is a surface controlled method that enables the deposition of material precise angstrom-level thickness with excellent uniformity, and demonstrates unique advantages in the application of surface coatings on cathode and anode materials of batteries.[13] Although single-crystalline Ni-rich cathode with a coating layer by ALD enables the suppression of grain boundary cracking due to internal stress and thus improve the structural stability and electrochemical performance,[13a, 13e] few studies elucidate the deterioration process and surface regulation mechanism of single-crystalline Ni-rich cathode. *In situ* electrochemical atomic force microscopy (EC-AFM) could monitor the dynamic evolution of the electrode morphology and its mechanical property by *in situ* scanning of the Derjaguin−Muller−Toporov (DMT) modulus at nanoscale.[4b, 14] Hence, it is expected that *in situ* EC-AFM could be used to understand the coupled electro-chemo-mechanical behaviors of single-crystalline Ni-rich cathode, and more importantly, to explore the structure-performance correlations of single-crystalline Ni-rich cathode based SSLBs.

In this work, via *in situ* EC-AFM, a single-crystalline LiNi$_{0.5}$Co$_{0.2}$Mn$_{0.3}$O$_2$ (NCM523) was used as a model material to reveal the dynamic degradation process and surface regulation mechanism of single-crystalline Ni-rich cathode in SSLBs, further understanding the structure-reactivity correlation. The generation of inhomogeneous cathode electrolyte interphase (CEI) and surface defects on surface of pristine single-crystalline NCM523 (P-NCM) particles are directly tracked, along with the decomposition of poly(vinylidene)fluoride (PVDF) & carbon and the formation of some unstable by-products with high DMT modulus. Conversely, an ionic conductor Li$_3$PO$_4$ (LPO) is introduced to coat single-crystalline NCM523 particle (L-NCM), leading to the uniform formation of CEI, which inhibits side reactions, maintains the initial structure of NCM523 and thus reinforces interfacial stability effectively. As a result, a modified cathode with improved cycling stability and rate performance in SSLBs at room temperature was achieved. These results reveal the surface degradation and regulation mechanism of single-crystalline NCM523 particles in SSLBs, and further provide a direct but vital proof for modification layer in reinforcing interfacial stability and dynamics, opening new avenues to the further optimization of battery materials and the establishment of interfacial engineering.

Results and Discussion

To enable safe and stable operation of SSLBs, surface regulation of single-crystalline NCM523 cathode for inhibition of side reaction and improvement of stability are required. The LPO modification layer is coated on the surface of single-crystalline NCM523 cathode undergoing ALD method, as schematically illustrated in Figure 1a. Aberration-corrected transmission electron microscopy (ACTEM) images and X-ray photoelectron spectroscopy (XPS) experiments were carried out to clarify the LPO had been successfully introduced on NCM523 particles (Figure 1b-c and e), and that of LPO coating layer with a thickness of ~ 6 nm is shown in Figure 1b. The coating process can not affect the layered structure (Figures 1c and S1a) and the microstructure (Figure 1f and S1b) of NCM523. X-ray diffraction

(XRD) patterns of the P-NCM and L-NCM show good retention of the NCM523 crystallinity without noticeable impurity phase caused by the ALD (Figure 1d).
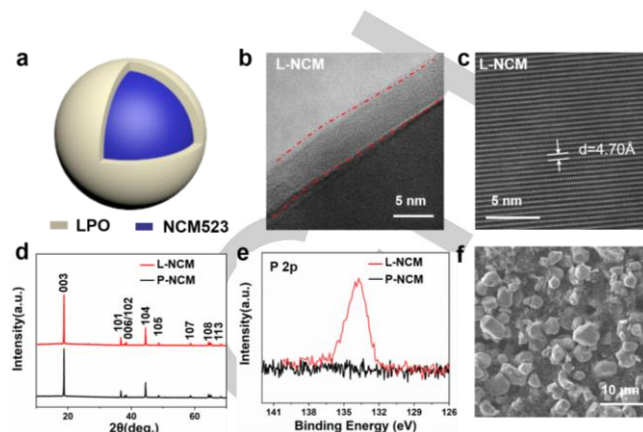
Figure 1. Schematic structure and characterizations of L-NCM. (a) Schematic illustration of the detailed structure of L-NCM. (b-c) The ACTEM images of the LPO coating layer on the surface of L-NCM. (d) XRD patterns of the L-NCM and the P-NCM. (e) P 2p XPS spectra of the L-NCM and the P-NCM. (f) Scanning electron microscopy (SEM) image of L-NCM.

In order to clarify the superiority of the coating process, cyclic voltammogram (CV) experiments at various sweep rates between 2.8 and 4.2 V were carried out to study the Li$^+$ diffusion kinetics in SSLBs. As shown in Figure S2, LPO layer is in favor of improving Li$^+$ diffusion obviously. Galvanostatic intermittent titration technique (GITT) experiments were further performed to reveal the variation of interfacial dynamics operated by LPO layer (Figure S3). The total polarization exhibits a significant reduction within LPO during charging, and voltage polarization of L-NCM is obviously lower at the later stage of charging. At the later stage of charging, high voltage charging process leads to obstruction of delithiation, and LPO layer facilitates a faster Li$^+$ diffusion in solid batteries, resulting in a relieved polarization and enhanced interfacial dynamics.

To study the surface degradation mechanism of single-crystalline Ni-rich cathode materials in a SSLB, *in situ* EC-AFM experiments were performed on P-NCM particles in a P-NCM/ipn-PEA/Li cell, as schematically illustrated in Figure 2 and Figure S4. Figure 2a indicates the observation region on a P-NCM cathode particle for AFM imaging. Figure 2b presents the typical CV of P-NCM/ipn-PEA/Li cell cycled in the voltage range of 2.8 - 4.2 V at a scan rate of 0.1 mV s^{-1}. The anodic peak at 3.9 V is related to the oxidation process of Ni ions (Ni^{2+}→Ni^{3+}/Ni^{4+}) and Co ions (Co^{3+}→Co^{4+}), as well as the deintercalation process of Li$^+$. The cathodic peak at 3.7 V is ascribed to the reverse reactions with the Li$^+$ intercalation into the cathode materials.[15] Figure 2c and S5 display the AFM images of P-NCM electrode at open circuit potential (OCP), and the flat region in the image is the single-crystalline NCM523 cathode particle surface with samples of block structure marked by white circle. Based on AFM imaging of composite electrode only contain carbon black and PVDF (Figure S6) and EDS mapping (Figure S7) of P-NCM electrode, these samples marked by white circle on P-NCM electrode surface mainly include PVDF and carbon black. The corresponding DMT modulus mapping of the P-NCM electrode shows that the average value is approximately 800 MPa, as exhibited in Figure 2c'. At the early stage of charging, no obvious

2
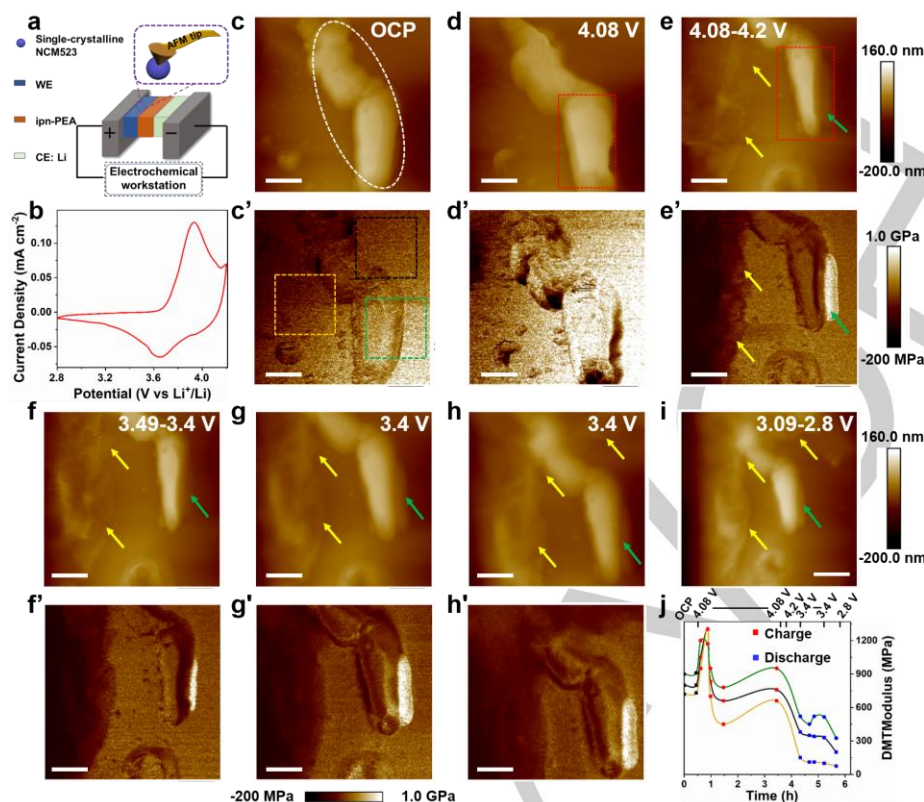
Figure 2. Degradation process of P-NCM particles in a SSLB. (a) Schematic illustration of the *in situ* electrochemical AFM cell. (b) Representative CV of the first cycle in a NCM523/ipn-PEA/Li cell at a sweep rate of 0.1 mV s⁻¹. *In situ* AFM images showing the topography (c-i) and mapping of the DMT modulus (c'-h') on the P-NCM electrode surface at OCP (c, c'), upon charging at 4.08 V (d, d'), during 4.08-4.2 V (e, e') and upon discharging during 3.49-3.4 V (f, f'), at 3.4 V (g-h, g'-h'), during 3.09-2.8 V (i). The scale bars are 200 nm in Figure c-h, c'-h', and the scale bar is 300 nm in Figure i. (j) Quantitatively measured average DMT modulus of the electrode surface at a certain position (black, yellow, green frame in Figure 2c') during cycling.

variation is observed (Figure 2d, 2d'). With further charging, it is worth noting that an amorphous film with lower DMT modulus grows locally on the side of the particle, as indicated by the yellow arrows in Figure 2e, e'. Meanwhile, these samples decompose and shrink gradually, marked by same red frame in Figure 2d, e and S8, accompanied by the generation of such products with higher DMT modulus, marked by green arrows in Figure 2e, e'. Upon discharging, this amorphous film grows, propagates and ultimately evolves into nonuniform partially-covered amorphous film, marked by yellow arrows in Figure 2f-i, and the DMT modulus of the on-site formed film decreases to ca. 100 MPa finally (Figure 2h', Figure S9). In our previous work, the decrease of DMT modulus may be owing to accumulation of the organic species, and the formation of inorganic species might lead to the increase of DMT modulus.[4b, 16] Figure 2j shows the evolution of the DMT modulus upon charging/discharging, of these *in situ* formed film at the three positions as indicated by the yellow, black and green frames in Figure 2c'. It is worth noting that the average DMT modulus of each region is obviously different, which further proves the difference in surface mechanical properties of the P-NCM electrode. Combined with previous research and above analyses, the observed on-site formed amorphous film is hereafter regarded as the CEI film on cathode particles.[4b]

The dynamics evolution of surface defects on P-NCM cathode particle is real-time recorded in Figure S10. These are some nano-structured samples mainly including PVDF and carbon black on P-NCM cathode surface at OCP as shown in Figure

S10a. When the cell is charged to 4.08 V, a "hole" appears on the electrode surface, as indicated by the green arrow in Figure S10b. With the charging proceeding, this "hole" gradually gets bigger (Figure S10c-d). Upon discharging, the generation process of another "hole" is captured on the observation region of electrode surface, marked by yellow arrows in Figure S9e-g. Finally, there are two surface defects in viewing area of P-NCM electrode after first cycle (Figure S10h).

The effect of surface defects on P-NCM cathode particles is further investigated by *in situ* AFM, as shown in Figure 3. Figure 3a shows the morphology of P-NCM cathode particle at OCP, where such samples mainly involving PVDF and carbon black are distributed on the surface marked by red circle, and the average DMT modulus is ca. 400 MPa (Figure S11a). When the cell is charged to 4.08 V, the degradation of these samples in red circle and the generation of surface defect like a "hole" marked by green arrow were observed in Figure 3b. When the cell is held at 4.08 V for 2 h, some inconspicuous flocculent products occur on the surface of particles, as marked by yellow arrow in Figure 3c, and these samples in red circle completely disappeared (Video S1). Motivated by some recent studies about influence of additive conductive carbon (carbon black) on the behaviour of cathode interphases,[17] disappearance of these samples may also be a result of acidic species attack on carbon & PVDF, resulting in side reaction between electrolyte and carbon & PVDF, and actively migrate to the cathode particles surface. As charging/discharging proceeds, the on-site film is slightly thicker and distributed locally on the surface of P-NCM when the

3
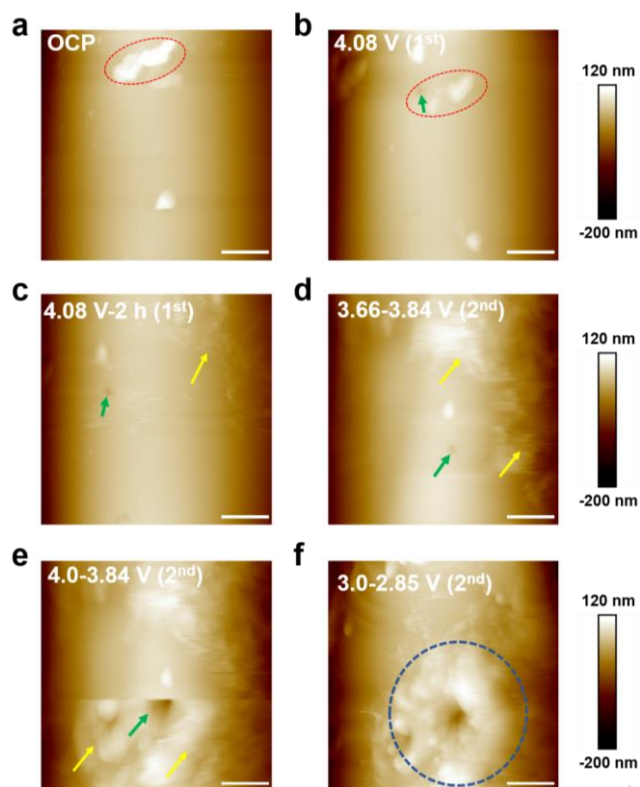
Figure 3. The formation of surface defects on P-NCM cathode particle surface in a SSLB. The *in situ* AFM images morphology of P-NCM electrode surface at OCP (a), upon charging (at 4.08 V 1st (b), 4.08V for 2h 1st, (c) 3.66-3.84 V 2nd (d)), and upon discharging (at 4.0-3.84 V 2nd (e), 3.0-2.85 V 2nd (f)). The scale bars are 160 nm.

potential was swept from 3.66 to 3.84 V at second cycle (Figure 3d), which can be identified as CEI film. As the experiment goes on, the "hole" on the electrode surface gets bigger greatly marked by green arrow in Figure 3e, and some products appear around the defect, as marked by yellow arrows in Figure 3e. Interestingly, along with the formation of these products, the corresponding DMT modulus mapping of these products suddenly increases to 250 MPa as indicated in Figure S11e. When the cell was discharged from 3.0 to 2.85 V at second cycle, these irregular products surrounded the surface defect on observation region of electrode, and the flower-like products left on the surface of electrode as marked by blue circle in Figure 3f. Such *in situ* observations of AFM reveal that the nonuniform CEI film generated on the P-NCM cathode particle surface, and the surface defect tend to appear on the surface of P-NCM particles simultaneously, accompanied by some irregular by-products forming around the surface defects.

The surface mechanism and dynamic evolution process of NCM523 single-crystalline cathode materials after LPO coating (L-NCM) in a SSLB are further investigated by *in situ* AFM, as shown in Figure 4. Figure 4a shows the CV of L-NCM/ipn-PEA/Li cell at a scan rate of 0.1 mV s^{-1}. Compared to P-NCM cathode, the CV curves of L-NCM cathode show sharp strong peaks (at ca. anodic 3.85 and cathodic 3.7 V), which are both related to the redox reaction processes of L-NCM. Combined with the *in situ* visualizations, the reaction mechanisms are further discussed below. An AFM image of the L-NCM cathode particle at OCP is

exhibited in Figure 4b, and the average value of DMT modulus of the electrode surface is ca. 120 MPa (Figure 4b'). Upon sweeping the potential from OCP to 4.08 V, no evident changes can be observed on the surfaces of the electrode particle. When the cell is held at 4.08 V for 1.0 h, some fibrous amorphous products with low DMT modulus form on the L-NCM electrode surface, as marked by yellow arrows in Figure 4c and c'. With the charging proceeding, this fibrous amorphous products increase gradually and ultimately evolve into planar amorphous film (Figure 4e). At this point, the average value of the DMT modulus of the electrode decreases to ca. 20 MPa (Figure 4e') as these products deposit. When the potential shifts from 4.08 to 4.2 V, this amorphous film is more evenly distributed on the surface of particles (Figure 4f), and the DMT modulus of electrode surface decreases to ca. 10 MPa (Figure S12). As the experiment progresses, the on-site formed film becomes smoother and denser, and eventually covers entire particle surface (Figure 4g), which could be drawn from the AFM images at different regions in Figure S13. Figure S14 shows the same results through another experiment, which confirm the this result is repeatable.

The quantitatively measured DMT modulus of L-NCM cathode particle at three certain positions, as indicated by the yellow, black and green frames in Figure 4b', during cycling is shown in Figure 4h. During the charging process, the average DMT modulus of these area decreases from 120 MPa (OCP) to 20 MPa (4.08 V), and then gradually decreases to 10 MPa (4.2 V). Subsequently, a slight increase in DMT modulus (50 MPa, 3.4 V) is recorded in real time upon discharging. As can be seen from the DMT modulus curves corresponding to the evolution processes of the on-site formed film (Figure 4h), the DMT modulus of three regions are essentially uniform except that there are slightly different during the formation process of the on-site formed film at charging to 4.08 V. In the combination of *in situ* AFM observations and above analyses, the growth of on-site formed film regarded as CEI films on the L-NCM cathode is real-time recorded. Comparatively speaking, the reaction process of the L-NCM electrode is more stable than that of the P-NCM electrode, which may be attributed to the regulation effect of modification layer for interfacial side reaction.

Besides, the *ex situ* XPS was conducted to delicately detect the chemical configuration and the degree of side reactions at the surface of P-NCM and L-NCM electrodes. Figure S15 displays the F 1s, O 1s and C 1s XPS spectra of the P-NCM and L-NCM electrodes at charging to 4.08 V. The assignments of the XPS peaks on F 1s, O 1s, and C 1s spectra are summarized in Table S1. In F 1s spectra, the L-NCM electrode shows a stronger peak at 685.5 eV compared to P-NCM electrode, as shown in Figure S15a, d, implying that the CEI film of L-NCM electrode is rich in LiF. As for O 1s and C 1s, the intensity of C=O/Li$_2$CO$_3$ and -CO$_3$ of P-NCM electrode surface is higher than L-NCM electrode, indicating the enrichment of Li$_2$CO$_3$ at P-NCM electrode surface. Meanwhile, the two peaks corresponding to C−O and O−H have higher intensity at L-NCM electrode surface. In the combination of *in situ* AFM observation and the chemical evolution by XPS, it is concluded that LiF-rich uniform and stable CEI film generates at the L-NCM cathode surface, while such unstable and inhomogeneous CEI with more Li$_2$CO$_3$ have produced on the P-NCM electrode surface, accompanied by generation of surface defects and interfacial side reaction. The barrier energy for diffusion of Li$^+$ on the surface of LiF (0.17 eV) is much lower than that on the surface of Li$_2$CO$_3$ (0.23 eV), indicating the faster

4
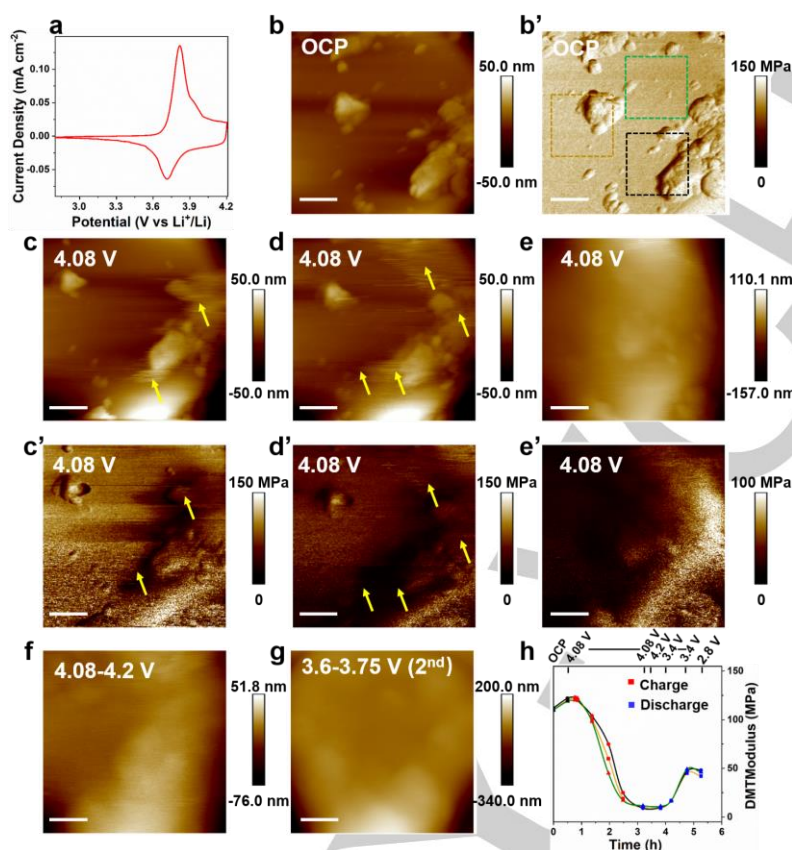
Figure 4. Surface Evolution of CEI film on the L-NCM cathode electrode in a SSLB. (a) Representative CV of the first cycle in a L-NCM/ipn-PEA/Li cell at a sweep rate of 0.1 mV s^{-1}. *In situ* AFM images showing the topography (b-g) and mapping of the DMT modulus (b'-e') on the L-NCM electrode surface at OCP (b, b'), upon charging at 4.08 V (c-e, c'-e'), during 4.08-4.2 V (f), during 3.6-3.75 V (g). The scale bars are 160 nm in Figure b-f, b'-e', and the scale bar is 300 nm in Figure g. (h) Quantitatively measured average DMT modulus of the electrode surface at a certain position (red, yellow, green frame in Figure 4b') during charging/discharging.

transport of Li$^+$ on LiF surface. It is thus considered that Li$_2$CO$_3$ plays the key role to impede Li$^+$ ion diffusion in cathode interphase layers rather than LiF.[18]

The surface degradation and interfacial regulation mechanism of the P-NCM and L-NCM electrodes with the ipn-PEA as the electrolyte upon charging/discharging were addressed on the basis of the aforementioned *in situ* AFM experiments and *ex situ* characterizations (Figure 5a). The inhomogeneous CEI and surface defects prefer to form on surface of P-NCM cathode particles, along with the decomposition of PVDF & carbon and the formation of some unstable by-products with high DMT modulus. This electrochemical behavior of the irregular generation of by-production and surface degradation may be related to the instability and poor contact of the cathode/electrolyte interface, which may further incur the irreversible dissolution of active material. And the different value of DMT modulus corresponding different components on P-NCM electrode surface might lead to uneven diffusion of the Li$^+$ ions and thus block ions transport. Conversely, an ionic conductor LPO was introduced to coat L-NCM particle by ALD, leading to the uniform formation of CEI, which inhibits side reactions, maintains the initial structure of NCM523 and thus reinforces interfacial stability effectively. Figure 5b and S16 show the electrochemical impedance spectroscopy (EIS) measurements of L-NCM and P-NCM electrode to probe the interfacial

resistance of the electrode at the first cycle and the 100th cycle. For detailed analyses, equivalent circuits were simulated to fit the experimental data (Table S2). The L-NCM cathode exhibits a slower charge-transfer resistance increasing than that of the P-NCM electrode during cycling, implying the LPO layer leads to polarization shrinkage and improved cycling stability, which is related to the uniformity of interfacial evolution process.[11a, 19] The LPO layer effectively matches the interface and induces the generation of LiF-rich stable CEI film, thus inhibiting the interfacial side reactions and enhancing interface dynamics which is consistent with the previous CV and AFM results.

To further clarify the superiority of modification layer in the electrochemical process in SSLBs, P-NCM or L-NCM cathodes and Li metal anodes with ipn-PEA solid electrolyte were assembled into full batteries. The initial charge and discharge curves for the P-NCM and L-NCM cathodes in solid batteries were tested at a low rate of 0.1 C between 2.8 and 4.2 V (Figure 5c). The reversible discharge capacities of P-NCM and L-NCM are 136.9 and 179.9 mA h·g^{-1}, respectively, and the L-NCM exhibits higher capacity. Meanwhile, it's observed that the L-NCM shows better rate performance from 0.1 C, and a capacity of 102.1 mA h g^{-1} can still be retained at a high rate of 2 C (Figure 5d). Figure 5e displays cycling performances of L-NCM and P-NCM over 100 cycles at a rate of 0.2 C, and the cycling stability of L-NCM is significantly improved. As schematically

5

illustrated in Figure 5c, the L-NCM cathode exhibits a capacity retention of 82.3% over 100 cycles (153 mA h g⁻¹) at a current rate of 0.2 C, while the P-NCM cathode remains only 67.8% of its initial capacity (83.9 mA h g⁻¹). Combining the results of *in situ* AFM and XPS, the improved cycling stability of L-NCM may be attributed to such stable and uniform LiF-rich CEI film on L-NCM cathode surface, and the excellent rate performance of L-NCM further proves that the LPO modification layer facilitates interfacial dynamics of SSLBs, which may be related to a consequence of this quality amorphous CEI protection and the rapid and uniform diffusion of the Li⁺ ions on the surface of electrode.
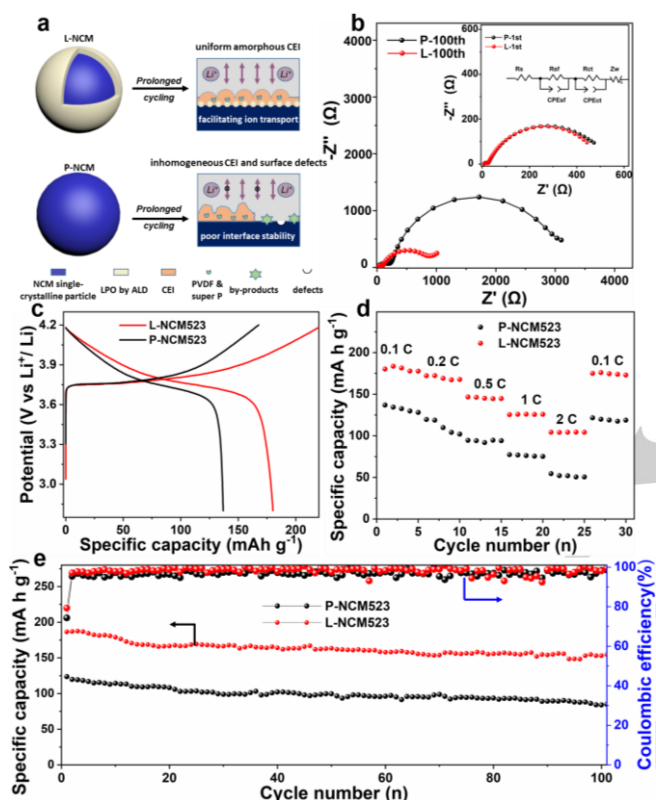
Figure 5. Electrochemical performances of P-NCM and L-NCM in SSLBs. (a) Schematic illustration of the surface degradation and interfacial regulation mechanism of the P-NCM and L-NCM electrodes with the ipn-PEA as the electrolyte upon charging/discharging. (b) Fitted impedance plots with inserted equivalent circuit derived from the first cycle and 100ᵗʰ cycle of P-NCM and L-NCM cathode. (c) Initial charge and discharge profiles of the two cathodes at a rate of 0.1 C. (d) Rate capabilities of the P-NCM and L-NCM cathode. (e) Cycling performances over 100 cycles at a rate of 0.2 C.

Conclusion

In summary, via *in situ* electrochemical AFM monitoring, we have successfully disclosed the dynamic degradation process, and surface regulation mechanism after LPO modification by ALD, of single-crystalline NCM523 cathode particles in working SSLBs. It is discovered that LPO layer play a key role in inducing LiF-rich stable CEI film on electrode surface and hampering interfacial side reaction, which determine the corresponding dynamic evolution process of surface morphology and mechanical property in SSLBs upon charging/discharging. Whereas, the formation of inhomogeneous and unstable CEI film

and the generation of surface defects on pristine single-crystalline NCM523 cathode were elucidated during cycling, which reveals the surface degradation of single-crystalline NCM523 cathode. The LPO coating mediates the surafce structure changes and dynamic evolution of the CEI film on single-crystalline NCM523 cathode, which further reduces resistance and relieves polarization at the interface between cathode and solid electrolyte. Such design can protect single-crystalline NCM523 cathode structure, alleviate side reactions, and enhance cycling stability and dynamic properties of SSLBs. These results provide straightforward evidence of the surface mechanism and structure−reactivity correlation of single-crystalline NCM523 cathode in SSLBs, and propose a facile and effective strategy to enhance cathode/solid electrolyte interface stability as well as dynamics for other solid batteries.

[1]   a) J. W. Choi, D. Aurbach, *Nat. Rev. Mater.* **2016**, 1, 16013; b) B. Dunn, H. Kamath, J. M. Tarascon, Science **2011**, 334, 928-935; c) S.-T. Myung, F. Maglia, K.-J. Park, C. S. Yoon, P. Lamp, S.-J. Kim, Y.-K. Sun, *ACS Energy Lett.* **2016**, 2, 196-223.

[2]   a) X. Han, Y. Gong, K. K. Fu, X. He, G. T. Hitz, J. Dai, A. Pearse, B. Liu, H. Wang, G. Rubloff, Y. Mo, V. Thangadurai, E. D. Wachsman, L. Hu, *Nat. Mater.* **2017**, 16, 572-579; b) R. Chen, Q. Li, X. Yu, L. Chen, H. Li, *Chem. Rev.* **2020**, 120, 6820-6877; c) A. Manthiram, X. Yu, S. Wang, *Nat. Rev. Mater.* **2017**, 2, 16103; d) J. Janek, W. G. Zeier, *Nat. Energy* **2016**, 1, 16141.

[3]   a) Y. Gong, Y. Chen, Q. Zhang, F. Meng, J. A. Shi, X. Liu, X. Liu, J. Zhang, H. Wang, J. Wang, Q. Yu, Z. Zhang, Q. Xu, R. Xiao, Y. S. Hu, L. Gu, H. Li, X. Huang, L. Chen, *Nat. Commun.* **2018**, 9, 3341; b) J. Y. Liang, X. D. Zhang, X. X. Zeng, M. Yan, Y. X. Yin, S. Xin, W. P. Wang, X. W. Wu, J. L. Shi, L. J. Wan, Y. G. Guo, *Angew. Chem. Int. Ed.* **2020**, 59, 6585-6589; c) S. Deng, X. Li, Z. Ren, W. Li, J. Luo, J. Liang, J. Liang, M. N. Banis, M. Li, Y. Zhao, X. Li, C. Wang, Y. Sun, Q. Sun, R. Li, Y. Hu, H. Huang, L. Zhang, S. Lu, J. Luo, X. Sun, *Energy Stor. Mater.* **2020**, 27, 117-123.

[4]   a) X. Cheng, Y. Li, T. Cao, R. Wu, M. Wang, H. Liu, X. Liu, J. Lu, Y. Zhang, *ACS Energy Lett.* **2021**, 6, 1703-1710; b) H. J. Guo, H. X. Wang, Y. J. Guo, G. X. Liu, J. Wan, Y. X. Song, X. A. Yang, F. F. Jia, F. Y. Wang, Y. G. Guo, R. Wen, L. J. Wan, *J. Am. Chem. Soc.* **2020**, 142, 20752-20762; c) Y. Su, J. Zhao, L. Chen, N. Li, Y. Lu, J. Dong, Y. Fang, S. Chen, F. Wu, *Chin. J. Chem.* **2021**, 39, 402-420; d) S. Lou, Q. Liu, F. Zhang, Q. Liu, Z. Yu, T. Mu, Y. Zhao, J. Borovilas, Y. Chen, M. Ge, X. Xiao, W. K. Lee, G. Yin, Y. Yang, X. Sun, J. Wang, *Nat. Commun.* **2020**, 11, 5700.

[5]   a) B. Yujing, J. Tao, L. L. Yuqin Wu, Yaobin Xu, Enyuan Hu, Bingbin Wu, Jiangtao Hu, Chongmin Wang, Ji-Guang Zhang, Yue Qi, Jie Xiao,

Science **2020**, 370, 1313-1317; b) A. J. Merryweather, C. Schnedermann, Q. Jacquet, C. P. Grey, A. Rao, *Nature* **2021**, 594, 522-528; c) R. Fantin, E. Trevisanello, R. Ruess, A. Pokle, G. Conforto, F. H. Richter, K. Volz, J. Janek, *Chem. Mater.* **2021**, 33, 2624-2634; d) L. Cheng, B. Zhang, S.-L. Su, L. Ming, Y. Zhao, X.-X. Tan, *RSC Advances* **2021**, 11, 124-128.

[6]   a) G. N. Qian, Y. T. Zhang, L. S. Li, R. X. Zhang, J. M. Xu, Z. J. Cheng, S. J. Xie, H. Wang, Q. L. Rao, Y. S. He, Y. B. Shen, L. W. Chen, M. Tang, Z. F. Ma, *Energy Stor. Mater.* **2020**, 27, 140-149; b) X. Ou, T. Liu, W. Zhong, X. Fan, X. Guo, X. Huang, L. Cao, J. Hu, B. Zhang, Y. S. Chu, G. Hu, Z. Lin, M. Dahbi, J. Alami, K. Amine, C. Yang, J. Lu, *Nat. Commun.* **2022,** 13, 2319.

[7]   a) X. Xu, H. Huo, J. Jian, L. Wang, H. Zhu, S. Xu, X. He, G. Yin, C. Du, X. Sun, Advanced Energy Materials 2019, 9, 1803961-1803963; b) H. Zhao, Y. Bai, H. Jin, J. Zhou, X. Wang, C. Wu, *Chem. Eng. J.* **2022**, 435; c) C. Wang, R. Zhang, C. Siu, M. Ge, K. Kisslinger, Y. Shin, H. L. Xin, *Nano Lett.* **2021**, 21, 9797-9804; d) F. Zhang, S. Lou, S. Li, Z. Yu, Q. Liu, A. Dai, C. Cao, M. F. Toney, M. Ge, X. Xiao, W.-K. Lee, Y. Yao, J. Deng, T. Liu, Y. Tang, G. Yin, J. Lu, D. Su, J. Wang, *Nat. Commun.* **2020**, 11, 3050.

[8]   a) X. Fan, G. Hu, B. Zhang, X. Ou, J. Zhang, W. Zhao, H. Jia, L. Zou, P. Li, Y. Yang, Nano Energy 2020, 70; b) R. Zhang, C. Wang, M. Ge, H. L. Xin, *Nano Lett* **2022**, 22, 3818-3824; c) E. Trevisanello, R. Ruess, G. Conforto, F. H. Richter, J. Janek, *Adv. Energy Mater.* **2021**,11, 2003400.

[9]   a) X. Fan, Y. Liu, X. Ou, J. Zhang, G. Hu, *Chem. Eng. J.* **2020,** 393, 124709; b) T. Kimijima, N. Zettsu, K. Yubuta, K. Hirata, K. Kami, K. Teshima, *J. Mater. Chem. A* **2016**, 4, 7289-7296.

[10]   a) W. Wang, L. Wu, Z. Li, K. Huang, J. Jiang, Z. Chen, X. Qi, H. Dou, X. Zhang, *ACS Appl. Energy Mater.* **2020**, 3, 12423-12432; b) X. M. Fan, Y. D. Huang, H. X. Wei, L. B. Tang, Z. J. He, C. Yan, J. Mao, K. H. Dai, J. C. Zheng, *Adv. Funct. Mater.* **2021**, 32; c) B. Zhang, J. Shen, Q. Wang, C. Hu, B. Luo, Y. Liu, Z. Xiao, X. Ou, *Energy Environ. Mater.* **2022,** DOI: 10.1002/eem2.12270. d) L. Ni, R. Guo, S. Fang, J. Chen, J. Gao, Y. Mei, S. Zhang, W. Deng, G. Zou, H. Hou, X. Ji, *eScience* **2022**, 2, 116-124

[11]   a) J. Y. Liang, X. X. Zeng, X. D. Zhang, P. F. Wang, J. Y. Ma, Y. X. Yin, X. W. Wu, Y. G. Guo, L. J. Wan, *J. Am. Chem. Soc.* 2018, 140, 6767-6770; b) M. J. Du, K. M. Liao, Q. Lu, Z. P. Shao, *Energy Environ. Sci.* **2019**, 12, 1780-1804; c) J. Liang, S. Hwang, S. Li, J. Luo, Y. Sun, Y. Zhao, Q. Sun, W. Li, M. Li, M. N. Banis, X. Li, R. Li, L. Zhang, S. Zhao, S. Lu, H. Huang, D. Su, X. Sun, *Nano Energy* **2020**, 78, 105107.

[12]   a) J. Y. Liang, X. X. Zeng, X. D. Zhang, T. T. Zuo, M. Yan, Y. X. Yin, J. L. Shi, X. W. Wu, Y. G. Guo, L. J. Wan, *J. Am. Chem. Soc.* **2019**, 141, 9165-9169; b) A. Zhou, J. Xu, X. Dai, B. Yang, Y. Lu, L. Wang, C. Fan, J. Li, *J. Power Sources* **2016,** 322, 10-16; c) L. P. Wang, X. D. Zhang, T. S. Wang, Y. X. Yin, J. L. Shi, C. R. Wang, Y. G. Guo, *Adv. Energy Mater.* **2018**, 8, 1801528.

[13]   a) X. Li, J. Liu, M. N. Banis, A. Lushington, R. Li, M. Cai, X. Sun, *Energy Environ. Sci.* **2014**, 7, 768-778; b) W. Liu, X. Li, D. Xiong, Y. Hao, J. Li, H. Kou, B. Yan, D. Li, S. Lu, A. Koo, K. Adair, X. Sun, *Nano Energy* **2018**, 44, 111-120; c) M. Amirmaleki, C. Cao, B. Wang, Y. Zhao, T. Cui, J. Tam, X. Sun, Y. Sun, T. Filleter, *Nanoscale* **2019**, 11, 18730-18738; d) B. Wang, J. Liu, Q. Sun, B. Xiao, R. Li, T.-K. Sham, X. Sun, *Adv. Mater. Interfaces* **2016**, 3, 1600369; e) M. Lee, W. Ahmad, D. W. Kim, K. M. Kwon, H. Y. Kwon, H.-B. Jang, S.-W. Noh, D.-H. Kim, S. J. A. Zaidi, H. Park, H. C. Lee, M. Abdul Basit, T. J. Park, *Chem. Mater.* **2022**, 34, 3539-3587.

[14]   a) Z. Z. Shen, Y. Z. Zhang, C. Zhou, R. Wen, L. J. Wan, *J. Am. Chem. Soc.* **2021**, 143, 21604-21612; b) J. Wan, Y. X. Song, W. P. Chen, H. J. Guo, FY. Shi, Y. J. Guo, J. L. Shi, Y. G. Guo, F. F. Jia, F. Y. Wang, R. Wen, L. J. Wan, *J. Am. Chem. Soc.* **2021,** 143, 839-848; c) S. Y. Lang, R. J. Xiao, L. Gu, Y. G. Guo, R. Wen, L. J. Wan, *J. Am. Chem. Soc.* **2018**, 140, 8147-8155.

[15]   a) M. Nie, Y.-F. Xia, Z.-B. Wang, F.-D. Yu, Y. Zhang, J. Wu, B. Wu, Ceramics International 2015, 41, 15185-15192; b) X. Jia, M. Yan, Z. Zhou, X. Chen, C. Yao, D. Li, D. Chen, Y. Chen, *Electrochim. Acta* **2017**, 254, 50-58.

[16]   R. Hiesgen, S. Sorgel, R. Costa, L. Carle, I. Galm, N. Canas, B. Pascucci, K. A. Friedrich, *Beilstein J Nanotechnol* **2013**, 4, 611-624.

[17]   a) W. Li, A. Dolocan, P. Oh, H. Celio, S. Park, J. Cho, A. Manthiram, Nat Commun 2017, 8, 14589. b) N. Membreño, K. Park, J. B. Goodenough, K. J. Stevenson, *Chem. Mater.* **2015**, 27, 3332-3340.

[18]   H. Duan, W. P. Chen, M. Fan, W. P. Wang, L. Yu, S. J. Tan, X. Chen, Q. Zhang, S. Xin, L. J. Wan, Y. G. Guo, *Angew. Chem. Int. Ed.* **2020**, 59, 12069-12075.

[19]   H. Kim, S. Lee, H. Cho, J. Kim, J. Lee, S. Park, S. H. Joo, S. H. Kim, Y. G. Cho, H. K. Song, S. K. Kwak, J. Cho, *Adv. Mater.* **2016**, 28, 4705-4712.

7

RESEARCH ARTICLE

WILEY-VCH

Entry for the Table of Contents
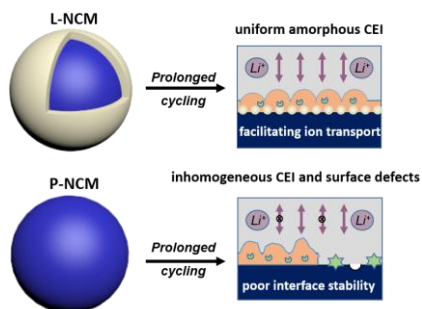
Insights into the surface mechanism on the single-crystalline LiNi$_{0.5}$Co$_{0.2}$Mn$_{0.3}$O$_2$ (SC-NCM) cathode are disclosed by *in situ* atomic force microscopy in quasi-solid-state batteries. Via atomic layer deposition, the Li$_3$PO$_4$ is introduced to coat SC-NCM, leading to the uniform formation of LiF-rich cathode electrolyte interphase and suppression of side reaction, which endows batteries with enhanced interfacial stability, durability and dynamics.